Egyptian Journal of Chemistry

http://ejchem.journals.ekb.eg/

Carbon Nanotubes from Agricultural Wastes: Effective Environmental Adsorbent

Hebat-Allah S. Tohamy, Mohamed El-Sakhawy*, Samir Kamel

Cellulose and Paper Department, National Research Centre, Cairo 12622, Egypt

Abstract

This research constitutes a relatively new area that has emerged from the synthesis of carbon nanotubes (CNTs) from hydrochars of agricultural wastes. The unwanted sugarcane bagasse (SCB), black liquor (BL), and mature beech pinewood sawdust (MW) waste in Egypt are used for CNTs preparation. SEM, TEM, and Raman spectra showed that the type of agricultural waste precursor affects the degree of wall graphitization and the number of tubes. Multiwalled carbon nanotubes (MWCNTs) with diameters of 5.39 - 19.78, 2.95 - 7.98, and 4.59 - 10.35 nm were prepared from the hydrochars of SCB, BL, and MW, respectively. CNT from SCB and BL consists of a small number of tubes and graphene (G) nanosheets. In comparison, that MW provided a larger number of tubes. The Ni^{2+} adsorption efficiency by CNTs under processing conditions was investigated. Our findings hinted that the adsorptions of Ni^{2+} to CNTs/SCB and CNTs/MW (R% = 81.85 and 79.78 respectively) were found to be much higher than that CNTs/BL (R%= 32.70). Our findings also hinted that the interaction between Ni^{2+} and CNTs/MW is an exothermic process (with a negative value of ΔH) while the adsorption between Ni^{2+} and CNTs/SCB and CNTs/BL is an endothermic process (with a positive value of ΔH).

1. Introduction

Ingestion of contaminated water is responsible for more deaths. For decades, industrialization and population expansion have negatively affected the environment; in turn, the environment poses a significant threat to human health [1-3]. Water pollutants could be divided into organic pollutants (e.g., oxygen demanding wastes, synthetic organic compounds, oil, pathogens, and nutrients) and inorganic pollutants (e.g., metal ions) [4]. Protecting the environment from dangerous waste pollution is the aim of this study. It is necessary to utilize inexpensive water purification techniques to purify contaminated water [5, 6]. For water treatment, various methods have been utilized for decades; the main problems are the high cost of operation and the problem of residual metal sludge disposal [7]. The adsorption process could be easily operated with low-energy and cheap requirements. The adsorption process depends on the adsorbent type, pollutants, and processing conditions. Batch reactors could be operated for water treatment [8]. Nanotechnology has opened a chance to research water treatment with cheap materials [5, 9, 10]. CNTs are 1D rolled graphene (G). They may be considered members of the fullerene structural family. They can be single-walled (SWCNT) and multiwalled (MWCNT). CNTs have potential applications in various fields. Modified CNT was used to separate and pre-concentrate heavy metal ions from food samples [11]. MWCNT is applied to the separation, preconcentration, and determination of traces of Fe(III) and Pb(II) content in water, food, and herbal plant samples [12. 13]. Also, Cd, Hg, and Pb in food packaging materials could be determined using CNT [14]. The chemical bonding involves entirely sp^2-hybrid carbon atoms, which provide outstanding properties [15]. The high price of carbon-based adsorbents encouraged researchers to research alternative adsorbents based on eco-friendly and bio-degradable lignocellulosic materials (LCMs) [16]. These polymers can be easily disposed of without damaging the environment [17]. Agricultural wastes can be easily recycled into worthy products and used in pollutant removal. Sugarcane bagasse (SCB), lignin (BL), and mature beech pine wood sawdust (MW) are LCMs with various active sites [8, 18].

This work investigates the synthesis and characterization of CNTs by a simple practical method from agro wastes. Furthermore, the obtained CNTs have been applied in Ni^{2+} removal from water, and the processing conditions have been studied in detail.

*Corresponding author e-mail: elsakhawy@yahoo.com

Receive Date: 22 February 2022, **Revise Date:** 17 May 2022, **Accept Date:** 12 June 2022, **First Publish Date:** 12 June 2022

DOI: 10.21608/EJCHEM.2022.123337.5511

2. Experimental

2.1. Materials and methods

Black liquor (BL) and sugarcane bagasse (SCB) were obtained from Qena Paper Industry Co., Upper Egypt. Mature beech pine wood sawdust (MW) was provided from a wood processing mill. The used raw materials (SCB, MW, and lignin) were air-dried, homogenized, and grinded to a mesh size of about 450 μ. The used chemicals and reagents employed in this study were of pure analytical grade and were used as received without any additional purification.

2.2. Lignin precipitation from black liquor (BL)

Lignin was precipitated from BL, which was produced from soda pulping of sugarcane bagasse (SCB) by acidification to pH 4 using 10% H_2SO_4. Lignin was filtered, washed till neutrality, and dried in the air [16].

2.3. Preparation of carbon nanotubes (CNTs)

5 g of carbon precursor (SCB, BL, or MW) was added into a mixture solution containing 10% $Fe_2(NO)_3{\cdot}9H_2O$, 10% $Ni(NO)_3{\cdot}6H_2O$, and 5% $(Co(NO)_3{\cdot}3H_2O)$. Then, 10 wt.% of urea in 20 ml H_2O was added to the previous mixture under vigorous stirring for 1 hr. The mixture was transferred into a stainless-steel reactor and heated in an electrical muffle at 180 °C for 3 hr. The hydrochar product was filtrated and washed with H_2O. Afterward, it was dried. In the next step, a wetness impregnation of $Al(OH)_3$ with 5 wt.% $Fe_2(NO)_3{\cdot}9H_2O$, $Ni(NO)_3{\cdot}6H_2O$ solutions and heated at 750 °C for 2 hr. in an electrical muffle. The obtained hydrochar was ground with this catalyst at a mass ratio of 10:1 and placed in the stainless-steel reactor at 800 °C for 1 hr. After cooling, the product was washed with 5M of HNO_3 and H_2SO_4, then with hot H_2O and dried. The synthesized CNTs from SCB, L, and MW were denoted as CNT/SCB, CNT/L, and CNT/MW, respectively [19]. The yields of CNTs from SCB, L, and MW were 4.77, 3.50, and 3.21%, respectively.

2.4. Characterization

CNTs were characterized by transmission electron microscopy (JEOL/JEM-2100 at 100K× magnification and an accelerating voltage of 120 kV). The SEM images were taken using Quanta/250-FEG connected to an energy-dispersive X-ray analyzer unit adjusted at an acceleration voltage of 30 kV. FTIR spectroscopy was recorded by Mattson-5000 (Unicam, United Kingdom) employing the KBr disk method in the wavenumber range of 4000–1000 cm^{-1}. While Raman spectra were recorded at an excitation laser wavelength of 532 nm using Raman confocal WITEC Focus Innovations Alpha-300 microscope. In addition, atomic absorption was studied on PerkinElmer-3110 (USA) to determine the quantity of Ni^{2+}.

The crystallinity was determined by Bruker D8 Advance X-ray diffractometer (Germany) using copper (Kα) radiation (1.5406 Å) at a 40 kV voltage and a 40 mA current. The sample was prepared using pressing tablets at a 1 mm thickness, and scans were carried out over Bragg angle (2θ) in the range of 5-80°. The thermogravimetric analysis (TGA) of the prepared polymer powders was studied on Perkin Elmer thermogravimetric analyzer. The specimen was heated to 1000 °C at a 10 °C/min rate under a nitrogen atmosphere. The thermal analysis data were recorded to estimate the activation energy (Ea) of the thermal decomposition using general equations (1) and (2) under the Coats-Redfern approach.

$$\log\left[\frac{1-(1-\alpha)^{1-n}}{T^2(1-n)}\right] = \log\frac{AR}{\beta E}\left[1-\frac{2RT}{E}\right] - \frac{E}{2.30} \quad (1)$$

$$\log\left[\frac{-\log(1-\alpha)}{T^2}\right] = \log\frac{AR}{\beta E}\left[1-\frac{2RT}{E}\right] - \frac{E}{2.303} \quad (2)$$

Where n is the order of degradation reaction, α is the fractional conversion, ß (K/min) is the heating rate, T (K) is the temperature, R (kJ/mol.K) is the gas constant, A (s^{-1}) is the frequency factor and E is the activation energy. According to the above equations (1) and (2), plotting a relationship between and 1/T employing different appropriate n values (from 0 to 3.0) should present a straight-line correlation, estimating the standard error (SE) and calculating the correlation coefficient (r). Ea was calculated from the slope (E/2.303R), whereas the frequency factor A was calculated from the intercept (log AR/ßE) by the most appropriate value of n [20, 21]. Enthalpy (ΔH), entropy (ΔS), and free energy change (ΔG) were estimated from equation (3).

$$\Delta H^* = E^* - RT;\ \Delta G^* = \Delta H^* - T\Delta S^* \text{ and } \Delta S \quad (3)$$

Where (h) is the Planck constant and (k) is the Boltzmann constant [8, 21-24].

Differential scanning calorimetry (DSC) scans were carried out by TA Instruments SDT Q600 V20.9 equipment. Dry N_2 was used as a purge gas. Specimens were heated to 600 °C at rates of 10 °C/min. The relative degree of crystallization (X_c) can be estimated from equation (4).

$$x_c(t) = \frac{A(t)}{A(\text{total})} \quad (4)$$

Where A(t) is the partial area of the peak at time t, and A(total) is the total peak area [25].

2.5. Adsorption evaluation of Ni^{2+}

The adsorption processes from solutions of Ni^{2+} were carried out by adding the CNTs (20 mg) into the Ni^{2+} solution (20 ml) of known initial concentration

(15 mg/l). The impact of the contact time was explored in the range from 15 to 90 min. The solution was stirred at a different temperature (298 to 328 K) for 30 min to estimate the effect of temperature. To study the effect of the initial concentration of Ni^{2+} on the adsorption efficiency, the elimination experiments were carried out with initial concentrations of 15, 20, 25, and 30 mg/g for 30 min and at 298 K. The final concentrations of the Ni^{2+} were reported employing atomic absorption spectrophotometer. The removal capacity percent (R%) of the CNTs was estimated by equation (5):

$$R\% = \frac{Co-Ct}{Co} \times 100 \quad (5)$$

Where C_0 is the initial concentration of Ni^{2+} in water and C_t is its final concentration after treatment.

2.6. Kinetic Modeling, Adsorption isotherms, and Thermodynamic parameters

The control rate mechanism was recorded to estimate the chemical reaction and mass transfer using pseudo-first and second-order order equations (6) and (7), respectively.

$$\ln\,[qe\,-\,qt] = \ln qe\,-\,K1t \quad (6)$$

$$\frac{t}{qt} = \frac{1}{K2qe2} + \frac{t}{qe} \quad (7)$$

where *qe* and *qt* are the adsorbed total content of Ni^{2+} (mg g^{-1}) at time *t*, K_1 (min^{-1}) is the first order adsorption rate constant, and K_2 (g/mg/min) is the pseudo second order adsorption rate constant. $qe_2$and K_2were estimated from the slope and intercept of plotting t/qt against t.

Langmuir and Freundlich's models are estimated from equations (8) and (9), respectively.

$$\frac{Ce}{qe} = \frac{1}{Kqm} + \frac{Ce}{qm} \quad (8)$$

$$\log qe = \log Kf + \frac{1}{n}\log Ce \quad (9)$$

where q_m (mg g^{-1}) is the maximum removal capacity and K_f is the adsorption capacity [8, 16].

ΔS; kJ mol^{-1}, ΔH; kJ mol^{-1}, K_d and ΔG; kJ mol^{-1} changes during adsorption can be investigated from the equation (10), (11), and (12). While the distribution coefficient (K_d) on the surface of CNTs was estimated from equation (11).

$$\ln Kd = \frac{\Delta S}{R} - \frac{\Delta H}{RT} \quad (10)$$

$$K_d = \frac{Ci-Ce}{Ce} \times \frac{V}{m} \quad (11)$$

$$\Delta G = -RT\ln K_d \quad (12)$$

where K_d is the distribution coefficient on the surface of CNTs. The values of ΔS and ΔH can be calculated from the intercept and slope by plotting $\ln K_d$ versus 1/T [8, 22, 23].

3. Results and discussion

3.1. Raman Spectroscopy

The G- bands located at 1593 cm^{-1} for CNTs/SCB is blue shifted to 1600 cm^{-1} for CNTs/BL, while it is red shifted to 1587 cm^{-1} for CNT**s**/MW (Fig. 1) [10]. The higher wavenumber of CNTs/BL's G-band improves the presence of sp^2 clusters [16, 22, 26]. The D- band (i.e., disorders) located at 1333, 1320, and 1361 cm^{-1} for CNTs/SCB, CNTs/BL, and CNTs/MW. Thus, a smaller I_D/I_G peak than 1 indicates a higher purity and a higher degree of graphitization [19, 26]. This result confirms that CNTs in CNTs/SCB, CNTs/BL, and CNTs/MW are well-graphitized, and the type of CNTs is multiwalled CNTs (MWCNTs) (Fig. 1) [19]. Also, the D- band's high intensity compared to the G-band of CNTs/BL proposes the presence of localized sp^3 defects within sp^2clusters. Otherwise, the G-band of CNTs/BL was wider than other samples due to the structural defects [16]. CNTs/MW has a high degree of wall graphitization (I_G/I_D~1.38).

1.1. FT-IR analysis

FT-IR spectra of CNTs/SCB, CNTs/BL, and CNTs/MW hydrochars are illustrated in Fig. 1. The peaks centered at 3419-3439, 1643-1644, 1398-1448, 1053-1121, and 1043-1129 cm^{-1} are attributed to stretching vibration modes of OH, C=O, O-C=O, C–O, and C–O–C groups, respectively [8, 22, 24]. The band at 2975 cm^{-1} can be attributed to C-H stretching, and this band was chosen as an internal standard to determine the relative absorbance (RA) [8]. The RA of the OH is 0.86, 0.59, and 0.79, while the intensity of the C=O is 0.97, 1.01, and 0.93 for CNTs/SCB, CNTs/BL, and CNTs/MW, respectively, which suggested that the produced CNTs is carboxylated one. Otherwise, RA of the C-O-C is 1.00, 1.05, and 1.01 for CNTs/SCB, CNTs/BL, and CNTs/MW, respectively. Generally, the high hydrophilic functional groups on the CNTs surface resulted in higher hydrophilicity (i.e. water dispersibility) [2].

The absorbance intensities at 1420-1430 and 900 cm^{-1} are attributed to the empirical crystallinity index (LOI) [16]. Measuring the LOI and MHBS revealed higher CNTs/SCB and CNTs/MW values, which may be due to their high degree of wall graphitization than CNTs/BL (Fig. 1).

1.2. Morphological Studies

CNTs/MW are produced from pyrolysis of hydrochar of MW, and their diameters are ranged between 4.59 and 10.35 nm. While needles like CNTs bundles (CNTs/SCB) and (CNTs/BL) grow between G nanosheets. The calculated diameters of the obtained CNTs/SCB and CNTs/BL varied from 5.39 to 19.78 and 2.95 to 7.98 nm, respectively. As a result, both CNTs/SCB and CNTs/BL are composed of a few CNTs and G nanosheets. This result confirms that CNTs can be considered a waving of G sheets [19]. The preparation of CNTs from MW provided well-defined MWCNTs (larger number of tubes) than CNTs/SCB and CNTs/BL (Fig. 2a-c).

Short accumulation of CNTs bundles is appeared in Fig. 2d, f. The bundles of CNTs/BL aren't appeared in SEM images due to their dryness (Fig.

2e). From EDX analysis, the observation of Si, S, Cl, Co, Fe, and Ni elements in the prepared CNTs reveals the impurity of the prepared CNTs.

1.1. XRD analysis

The prepared CNTs are composed of a few CNTs and G nanosheets. The G nanosheets have an amorphous peak at 2θ = 9.3° related to the (001) plane (Tohamy et al., 2021). XRD pattern of MWCNTs shows (002) diffraction peak at 2θ =25.5°, 22.5°, and 30.2° for CNTs/SCB, CNTs/BL, and CNTs/MW, respectively. The X-ray pattern of CNTs/MW is sharper than CNTs/SCB and CNTs/BL (Fig. 3). This may be due to the greater number of CNTs in CNTs/MW, the highly graphitic structure than other samples, and the multiwall of CNTs/MW in nature (see TEM and Raman section) [27].

The XRD's CrI% values agree with the MHBS and LOI values. The d-spacing in CNTs/SCB and CNTs/BL is increased than CNTs/MW. This increase in d-spacing may be due to the functional groups inserted in the interlayers of G [28, 29]. This preparation method proves a successful CNT production without supporting gases or vacuum and by using lower preparation temperature compared with other techniques such as arc discharge or laser ablation methods [30].

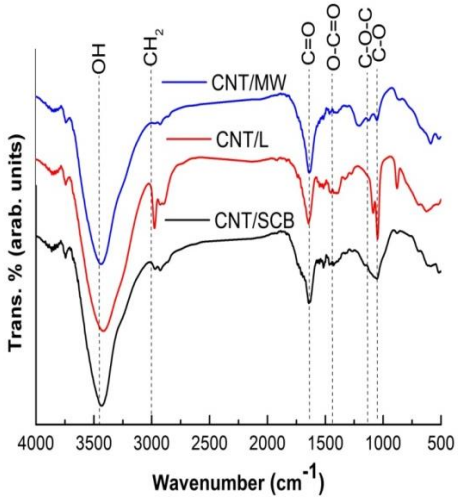

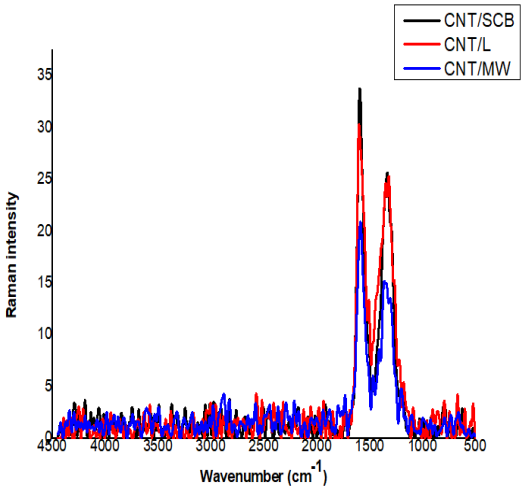

Sample	D- band (cm^{-1})	G- band (cm^{-1})	FWHM band (cm^{-1})	I_D/I_G	I_G/I_D	Crystal diameter (nm)	A_{1425}/A_{900} (LOI)	(A_{OH}/A_{CH})
CNTs/SCB	1333	1593	79.5	0.74	1.35	25.95	1.01	0.86
CNTs/L	1320	1600	86	0.85	1.18	22.68	0.96	0.59
CNTs/MW	1361	1587	79	0.73	1.38	26.53	0.98	0.79

Fig. 1 Raman (left), FTIR (right) spectra, ID/IG, and H-bond strength of CNTs/SCB, and CNTs/BL, and CNTs/MW.

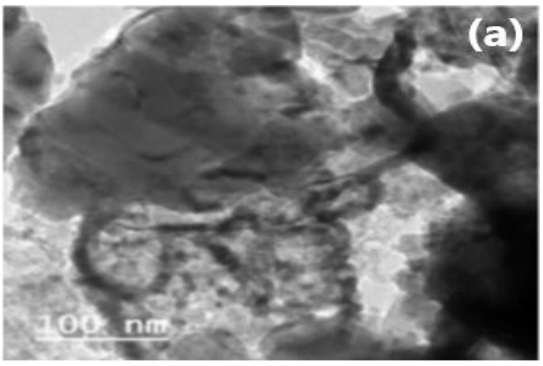

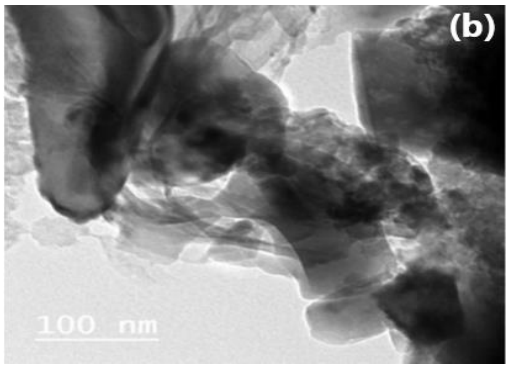

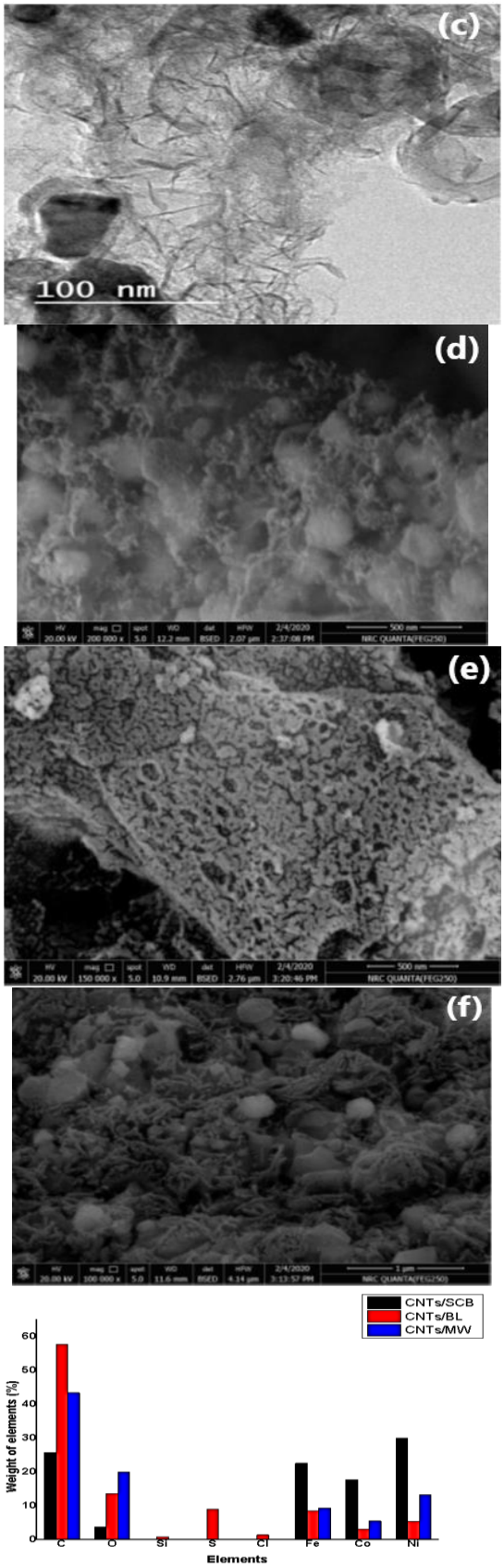

Fig. 2 TEM (a, b, and c) and SEM (d, e, and f) images of CNTs/SCB, CNTs/BL, CNTs/MW respectively as well as EDX histogram.

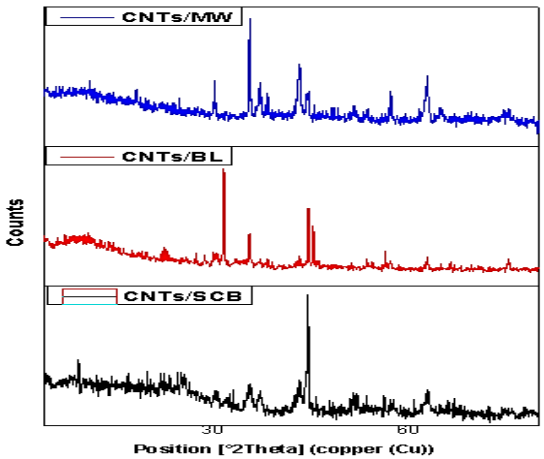

	CNTs/SCB	CNTs/BL	CNTs/MW
CrI. (%)	16.06	4.55	14.63
$d_{spacing}$ (nm)	42.83	45.62	39.83

Fig. 3. XRD patterns, crystallinity index, and interlayer spacing of the prepared CNTs.

1.2. Thermal properties

The TGA results for CNTs/SCB, CNTs/BL, and CNTs/MW are given in Fig. 4a-c. TGA study of CNTs/SCB shows no weight variation up to 1000°C. This indicating no bond splitting takes place [31]. In general, the decomposition profile of CNTs/MW displayed two decomposition stages, while CNTs/BL showed three decomposition stages. The chemical composition between CNTs/SCB, CNTs/BL, and CNTs/MW was the main reason for the monitored differences in thermal stability and thermal decomposition behavior. The sudden temperature change produces a thermal shock taking the functional groups out from the lattice structure of CNTs in the form of water vapor, CO, and CO_2. The TGA CNTs/BL and CNTs/MW at 1000 °C showed a weight loss of 76.65 and 91.57%, respectively, indicating the existence of non-volatile constituents. The thermal decomposition of CNTs/BL can be monitored in three major stages. The initial weight loss stage was monitored in the range of 35.94-165.24°C (average weight loss of 9.27%), most probably due to losing the moisture content. The second weight loss stage was between 165.24-480.62°C (average weight loss of 5.09%). This was caused by several concurrent processes, such as dehydroxylation, in combination with pyrolytic fragmentation to result in aromatized moieties and volatile products. The third decomposition step was between 489.18-996.29°C (average weight loss of 62.29%), which was assigned to the decomposition of the carbonaceous residues [20, 23].

As demonstrated in Fig. 4, the thermal decomposition processes of CNTs/MW can be divided into two main decomposition stages. The first weight loss was attributed to moisture loss in the

temperature range between 36.12-68.93°C (average weight loss of 2.98%). The first weight loss stage was followed by the main (second) decomposition stage between 199.12-978.16°C (average weight loss of 88.58%). The weight loss was mainly attributed to the fragmentation accompanying the pyrolytic decomposition, which created aromatized moieties and decomposed the carbonaceous residues [8, 21, 24].

Table 1 Thermodynamic and thermoanalytical screening of the thermal decomposition stages for CNTs/BL and CNTs/MW.

Sample	CNTs/BL			CNTs/MW	
Stage	1st	2nd	3rd	1st	2nd
TGA range (°C)	35.94-165.24	165.24 -480.62	489.18-996.29	36.12-68.93	199.12-978.16
Mass loss (%)	9.27	5.09	62.29	2.98	88.58
N	0.5	0.5	0.5	0.5	0.5
R^2	0.997	0.994	0.996	0.996	0.994
SE	0.009776	0.005615	0.41212	0.0004331	0.044128
E (kJ mol^{-1})	6.101	7.18	42.64	5.98	8.29
∑Ea	55.92			14.27	
Residual weight (%)	76.65			91.57	

The three kinds of CNTs/SCB, CNTs/BL, and CNTs/MW samples with the varying origin of agricultural wastes were subjected to DSC analysis (Fig. 4d-f). It was shown that the type of waste has a considerable influence on crystallization and melting behaviors for the three different CNTs. CNTs have two melting temperatures (T_m) denoted as T_{m1} and T_{m2}. The DSC curves of CNTs/SCB, CNTs/BL, and CNTs/MW showed one endothermic peak at 409.71, 85.60, and 61.52 °C, attributed to the removal of moisture and T_{m1}. While another endothermic peak at 592.02, 589.20, and 588.95 °C was attributed to the CNTs decomposition (Table 2).

These changes in the temperature of thermal transitions confirmed the difference in CNTs prepared from different agro-wastes. The DSC curve recorded for CNTs/MW showed a glassy thermoplastic material with glass transition (T_g) at 398.12 °C. As seen, preparing high degree MWCNTs in the case of CNTs/MW results in a decrease in T_m temperatures. This means the incorporation of MWCNTs significantly disrupted the crystallization process. The degree of crystallinity (X_c) for CNTs is shown in Table 2. It proves that CNTs/MW (MWCNT) caused an easygoing growth in crystals [25]. DSC results showed that as the temperature was increased, the CNT was triggered for an endothermic reaction.

Table 2 Melting temperatures and crystallinity for the prepared CNTs.

Sample	T_{m1}	T_{m2}	T_g	X_c
CNTs/SCB	409.71	592.02	-	63.09
CNTs/BL	85.60	589.20	-	31.75
CNTs/MW	61.52	588.95	398.12	32.86

1.1. Adsorption study

1.1.1. Optimization of the adsorption conditions

From the effect of the contact time study, it was clarified that the removal was found to be quickly rising due to the presence of active sites. Then, the removal became slow, and there was no remarkable rise in the adsorption rate spotted after 15, 75, and 75 min. for CNTs/SCB, CNTs/BL and CNTs/MW, respectively (Fig. 5a).

The effect of the temperature study showed when the temperature rises, the removal of Ni^{2+} by CNTs/SCB and CNTs/BL increases (endothermic process). When the temperature reduces, the removal of Ni^{2+} by CNTs/MW surface decreases (exothermic process) (Fig. 5b) [8, 16, 24].

Furthermore, the removal of CNTs/SCB, CNTs/BL, and CNTs/MW increased with increasing the initial concentration, defeating all mass transfer resistances (Fig. 5c) [8].

1.1.2. Kinetic Modeling, Adsorption isotherm, and Thermodynamic parameters

The pseudo-second-order model suited the adsorption data better than the first-order one for all samples (Table 3). This means that surface processes involving chemisorptions and physisorption share in the adsorption of Ni^{2+} by CNT/SCB, CNT/L, and CNT/MW (Fig. 6) [8, 16].

CNT/SCB and CNT/L isotherms best fit the Langmuir (i.e., monolayer adsorption), while CNT/MW fit the Freundlich isotherm model (i.e., multilayer adsorption) (Fig. 6, Table 3) [8, 22].

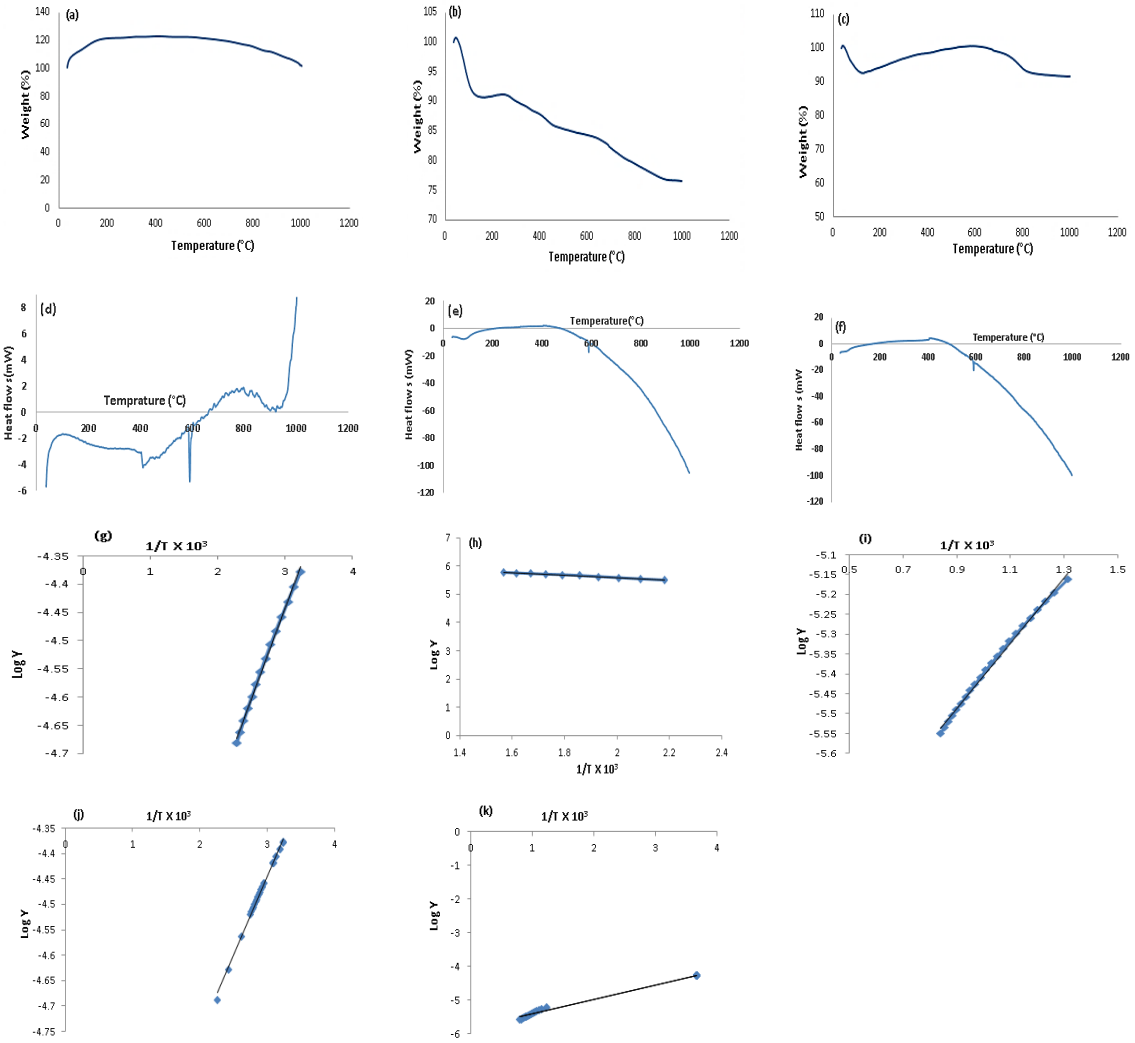

Fig. 4 TGA (a-c) and DSC (d-f) of CNTs/SCB, CNTs/BL, and CNTs/MW and thermograms of 1st, 2nd, 3rd stages of CNTs/BL (g-i) and 1st and 2nd stages of CNTs/MW (j-k).

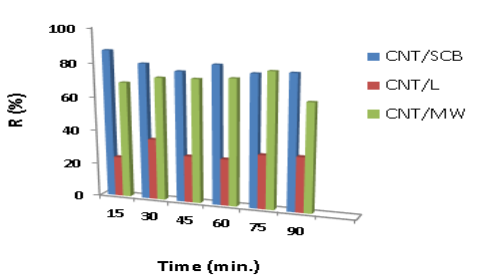

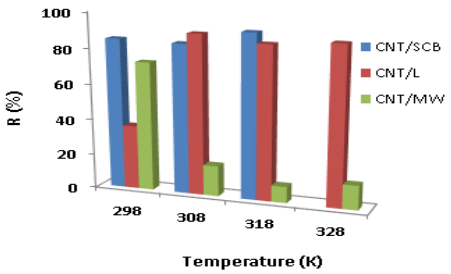

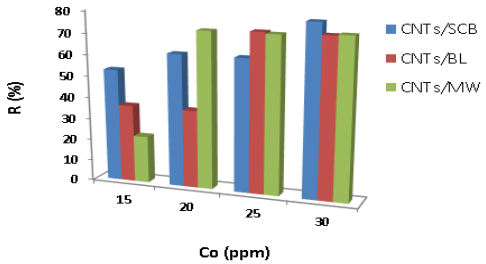

Fig. 5. Effect of contact time (a), temperature (b), initial Ni^{2+} concentration (c) on removal capacity by CNTs/SCB, CNTs/BL, and CNTs/MW.

The negative value of ΔH in CNT/MW is due to the exothermic process, while the positive value in CNT/SCB and CNT/L samples is due to the endothermic process. The negative values of ΔG indicate spontaneous adsorption. The ΔS positive

CNT/SCB and CNT/L values indicate the randomness (Table 3). While the ΔS negative value in CNT/MW indicates the decreased randomness at the CNT–solution interface [8, 24]. From all these results, it could be concluded that the change more influenced the adsorption of CNT in solution temperature.

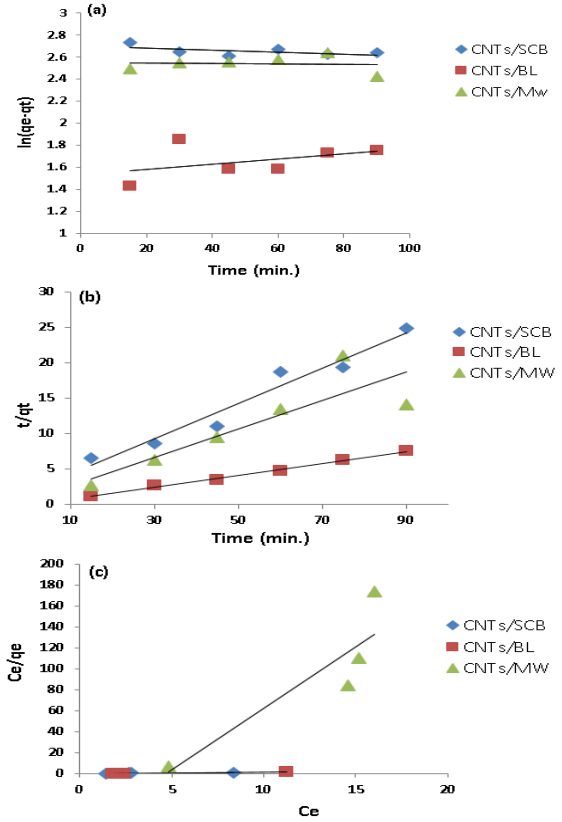

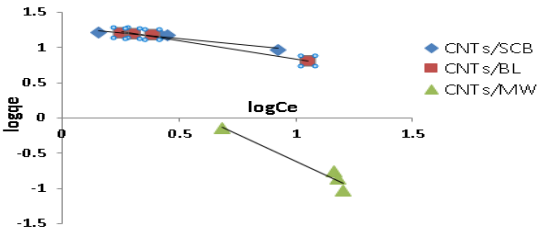

Fig. 6. Kinetic parameters of (a) Pseudo-first-order, (b) Pseudo-second-order reaction, (c) Langmuir isotherm and (d) Freundlich isotherm of Ni^{2+} on CNTs/SCB, CNTs/BL, and CNTs/MW surfaces. Initial concentration 15 mg/l; adsorbent dosage: 20 mg; time: 30 min.

Conclusions

The above research work concludes that SCB, L, and MW wastes are a great alternative raw material that can be used to produce CNTs sustainably. CNTs prepared by hydrothermal treatment of agricultural waste raw material followed by pyrolysis of hydrochar product. It can be used as an eco-friendly way of producing CNTs, and further research can be conducted to increase the number of CNTs produced. Raman spectra result confirms that CNTs in CNT/SCB, CNT/L, and CNT/MW are well-graphitized, and the type of CNTs is MWCNTs. The G band was much broader in the case of the CNT/L spectrum compared with other samples due to the structural imperfections. On the other hand, CNT/MW has a high degree of wall graphitization.

Table 3. Rate constants and correlation coefficients associated with the pseudo-first-order and the pseudo-second-order rate, Langmuir & Freundlich models parameters for adsorption of Ni^{2+}. (initial concentration 15 mg/L).

Kinetic model	Parameter		Adsorbent		
			CNTs/SCB	CNTs/BL	CNTs/MW
Pseudo first order	$q_{exp.}$		15.34	6.37	14.03
	$q_{calc.}$		14.90	4.64	12.77
	K_1		$92X10^{-4}$	$43X10^{-3}$	$12X10^{-4}$
	R^2		0.349	0.945	0.911
Pseudo second order	$q_{calc.}$		4.00	11.84	4.98
	K_2		0.1414	0.7123	0.3158
	R^2		0.957	0.994	0.964
Langmuir	q_m (mg/ g)		8.23	5.63	0.08
	R^2		0.993	0.998	0.805
Freundlich	K_f ($mg^{(1-1/n)}$ g^{-1} $L^{1/n}$)		3.64	3.87	2.47
	R^2		0.926	0.988	0.949
Thermodynamic parameters	ΔS (kJ/ mole)		0.19	0.21	-0.25
	ΔH(kJ/ mole)		$57X10^4$	$62X10^3$	$-76X10^3$
	ΔG (kJ/ mole)	298 K	-0.26	1.41	-2.43
		308 K	-4.43	-5.58	4.01
		318 K	-4.40	-4.84	6.05
		328 K	-6.64	-5.57	5.01

From TEM, it can be said that both CNT/SCB and CNT/L are composed of a few CNTs and G nanosheets. CNT/SCB, CNT/L, and CNT/MW diameters are ranged between 2.95-19.78 nm. SEM shows an accumulation of short CNTs bundles for CNT/SCB and CNT/MW.

Our findings on the Ni^{2+} adsorption study hinted that the adsorption of Ni^{2+} to CNT/SCB and CNT/MW (%R= 81.85 and 79.78, respectively) was found to be much higher than CNT/L (%R= 32.70). The interaction between Ni^{2+}, CNT/MW is an exothermic process (negative ΔH), while the adsorption between Ni^{2+} and CNT/SCB and CNT/L is an endothermic process (positive ΔH).

Conflict of Interests

The authors declare that they have no conflict with interests.

Acknowledgment

This paper is based upon work supported by Science. Technology & Innovation Funding Authority (STDF) under grant (45892).

References

[1] Liu S. Graphene oxide and graphene-based catalysts in photochemical reactions, (Doctoral dissertation, Curtin University), 2013.

[2] Wang J. and Chen B. Adsorption and coadsorption of organic pollutants and a heavy metal by graphene oxide and reduced graphene materials, *Chemical Engineering Journal*, **281**, 379-388 (2015).

[3] Wang S., Sun H., Ang H.-M. and Tadé M. Adsorptive remediation of environmental pollutants using novel graphene-based nanomaterials, *Chemical engineering journal*, **226**, 336-347 (2013).

[4] Ghangrekar M. and Chatterjee P. Water pollutants classification and its effects on environment, In *Carbon nanotubes for clean water* (pp. 11-26). Springer, Cham. 2018.

[5] Aghigh A., Alizadeh V., Wong H.Y., Islam M.S., Amin N. and Zaman M. Recent advances in utilization of graphene for filtration and desalination of water: a review, *Desalination*, **365**, 389-397 (2015).

[6] Wang Z., Dou B., Zheng L., Zhang G., Liu Z. and Hao Z. Effective desalination by capacitive deionization with functional graphene nanocomposite as novel electrode material, *Desalination*, **299**, 96-102 (2012).

[7] Baysal, A., Ozbek, N. and Akman, S. Determination of trace metals in waste water and their removal processes, *Waste Water-Treatment Technologies and Recent Analytical Developments*, Einschlag, F & Carlos, L (eds.). IntechOpen, London. 10.5772/3443, 145-171 (2013).

[8] Tohamy H.-A. S., El-Sakhawy M. and Kamel S. Carboxymethyl Cellulose-Grafted Graphene Oxide/Polyethylene Glycol for Efficient Ni (II) Adsorption, *Journal of Polymers and the Environment*, **29**, 859-870 (2021).

[9] Kamel S., El-Sakhawy M., Anis B. and Tohamy H.-A. S. Graphene: Structure, Synthesis, and Characterization; a brief review, *Egyptian Journal of Chemistry*, **63**, Special Issue (Part 2) Innovation in Chemistry, 593-608 (2020).

[10] Xu P., Zeng G.M., Huang D.L., Feng C.L., Hu S., Zhao M.H., Lai C., Wei Z., Huang C. and Xie G.X. Use of iron oxide nanomaterials in wastewater treatment: a review, *Science of the Total Environment*, **424**, 1-10 (2012).

[11] ALOthman Z. A., Habila M., Yilmaz E. and Soylak M. Solid phase extraction of Cd (II), Pb (II), Zn (II) and Ni (II) from food samples using multiwalled carbon nanotubes impregnated with 4-(2-thiazolylazo) resorcinol, Microchimica Acta, 177(3), 397-403(2012).

[12] Soylak M., and Unsal Y. E. Solid-phase extraction of heavy metal ions on bucky tubes disc in natural water and herbal plant samples, Environmental monitoring and assessment, 181(1), 577-586(2011).

[13] Soylak M. and Unsal Y. E. Determination of traces of iron and lead in food and water samples after preconcentration on multiwalled carbon nanotubes, Journal of Aoac International, 95(4), 1183-1188 (2012).

[14] Zhang L. and Fan, Z. Carbon Nanotube-Coated Capillary Micro-extraction Combined with Graphite Furnace Atomic Absorption Spectrometry for the Determination of Cd, Hg, and Pb in Food Packaging Materials, Atomic Spectroscopy, 34(1), 26-30 (2013).

[15] Kharisov B.I. and Kharissova O.V. *Carbon Allotro*pes: Metal-Complex Chemistry, Properties and Applications. Springer, 2019. https://doi.org/10.1007/978-3-030-03505-1

[16] Tohamy H.-A. S., Anis B., Youssef M. A., Abdallah A. E., El-Sakhawy M. and Kamel S. Preparation of eco-friendly graphene oxide from agricultural wastes for water treatment, *Desalination and Water Treatment*, **191**, 250-262 (2020).

[17] Dong P., Prasanth R., Xu F., Wang X., Li B. and Shankar R. Eco-friendly polymer Nanocomposite—properties and processing, In *Eco-friendly Polymer Nanocomposites* (pp. 1-15). Springer, New Delhi.Springer, 2015.

[18] Xu M. and McKay G. Removal of heavy metals, lead, cadmium, and zinc, using adsorption processes by cost-effective adsorbents, In *Adsorption processes for water treatment and*

purification (pp. 109-138). Springer, Cham., 2017.

[19] Lotfy V.F., Fathy N.A. and Basta A.H. Novel approach for synthesizing different shapes of carbon nanotubes from rice straw residue, *Journal of Environmental Chemical Engineering*, **6**(5), 6263-6274 (2018).

[20] El-Sakhawy M., Tohamy H.-A. S., Salama A. and Kamel S. Thermal properties of carboxymethyl cellulose acetate butyrate, *Cellulose Chemistry and Technology*, **53** , 667-675 (2019).

[21] Tohamy, H.-A. S., Kamel, S., El-Sakhawy, M., Youssef, M. A., Abdallah, A. E. and Anis, B. Thermal properties of graphene oxide prepared from different agricultural wastes, *Egyptian Journal of Chemistry*, **63**, 10 (2020), 8-10.

[22] Tohamy H.-A.-S., El-Sakhawy M. and Kamel S. Development of Magnetite/Graphene Oxide Hydrogels from Agricultural Wastes for Water Treatment, *Journal of Renewable Materials*, **10**(7), 1889-1909 (2022). doi: 10.32604/jrm.2022.019211

[23] Tohamy H.-A. S., Kamel S., El-Sakhawy M. Graphene oxide functionalized by ethylene diamine tetra-acetic acid (EDTA) by a hydrothermal process as an adsorbent for nickel ions, *Cellulose Chemistry and Technology*,**55**, 417-432 (2021).

[24] Tohamy H.-A.S., El-Sakhawy M. and Kamel S. Development of graphene oxide-based styrene/acrylic elastomeric disks from sugarcane bagasse as adsorbents of Nickel (II) ions, *Journal of Polymer Research*, **29**(3), 75 (2022). https://doi.org/10.1007/s10965-021-02830-5

[25] Jin J., Song M. and Pan F. A DSC study of effect of carbon nanotubes on crystallisation behaviour of poly (ethylene oxide), *Thermochimica acta*, **456**, 25-3 (2007).

[26] Hu Z., Hu Y., Chen Q., Duan X. and Peng L.-M. Synthesis and characterizations of amorphous carbon nanotubes by pyrolysis of ferrocene confined within AAM templates, *The Journal of Physical Chemistry B*, **110**(16), 8263-8267 (2006).

[27] Zhou L., Fang S., Tang J., Gao L. and Yang J. Synthesis and characterization of multiwalled carbon nanotube/polyurethane composites via surface modification multiwalled carbon nanotubes using silane coupling agent, *Polymer composites*, **33**(11), 1866-1873 (2012).

[28] Serag E., El Nemr A. and El-Maghraby A. Synthesis of highly effective novel graphene oxide-polyethylene glycol-polyvinyl alcohol nanocomposite hydrogel for copper removal, *Journal of Water and Environmental Nanotechnology*, **2**(4), 223-234 (2017).

[29] Vu H.C., Dwivedi A.D., Le T.T., Seo S.-H., Kim E.-J. and Chang Y.-S. Magnetite graphene oxide encapsulated in alginate beads for enhanced adsorption of Cr (VI) and As (V) from aqueous solutions: role of crosslinking metal cations in pH control, *Chemical Engineering Journal*, **307**, 220-229 (2017).

[30] Pandey P. and Dahiya M. Carbon nanotubes: Types, methods of preparation and applications, Carbon, 1(4), 15-21 (2016).

[31] Pang L.S., Saxby J.D. and Chatfield S.P. Thermogravimetric analysis of carbon nanotubes and nanoparticles, *The Journal of Physical Chemistry*, **97**(27), 6941-6942 (1993).